



Low-energy electron transport in gold: mesoscopic potential calculation and its impact on electron emission yields

Ricardo Ramos, Floriane Poignant, Chen-Hui Chan, A. Ipatov, B. Gervais,
Elise Dumont, David Loffreda, Michaël Beuve

► To cite this version:

Ricardo Ramos, Floriane Poignant, Chen-Hui Chan, A. Ipatov, B. Gervais, et al.. Low-energy electron transport in gold: mesoscopic potential calculation and its impact on electron emission yields. *Eur.Phys.J.Plus*, 2021, 136 (3), pp.345. 10.1140/epjp/s13360-021-01318-x . hal-03186180

HAL Id: hal-03186180

<https://hal.science/hal-03186180>

Submitted on 8 Nov 2021

HAL is a multi-disciplinary open access archive for the deposit and dissemination of scientific research documents, whether they are published or not. The documents may come from teaching and research institutions in France or abroad, or from public or private research centers.

L'archive ouverte pluridisciplinaire **HAL**, est destinée au dépôt et à la diffusion de documents scientifiques de niveau recherche, publiés ou non, émanant des établissements d'enseignement et de recherche français ou étrangers, des laboratoires publics ou privés.

Low-energy electron transport in gold: mesoscopic potential calculation and its impact on electron emission yields.

R. Ramos¹, F. Poignant¹, C.-H. Chan³, A. Ipatov², B. Gervais⁴, D. Loffreda³, E. Dumont³, M. Beuve¹.

¹ Univ Lyon, Université Claude Bernard Lyon 1, CNRS/IN2P3, Institut de Physique des Deux Infinis de Lyon, 69622 Villeurbanne, France.

² St. Petersburg National Research Academic University RAS, 194021 St. Petersburg.

³ Univ Lyon, Ens de Lyon, CNRS UMR 5182, Université Claude Bernard Lyon 1, Laboratoire de Chimie, F-69342 Lyon, France.

⁴ CIMAP, unité mixte CEA-CNRS-ENSICAEN-USBN 6252 BP 5133, F-14070 Caen, Cedex 05, France.

Abstract

In a previous work, we extended and benchmarked the MDM Monte Carlo code with available data for gold metallic media irradiated by electron beams.

In this paper, we worked with the aim of improving the cross sections on which our Monte Carlo simulation is based, and which are essential for an accurate description of the transport of electrons in gold. The mesoscopic potential of solid gold has been predicted and its sensitivity toward electron emission has been evaluated. This potential was derived from the calculation of the electrostatic and atomistic potential by Density Functional Theory and used to calculate inelastic inverse mean free path for electron transport. After integrating these results into our Monte Carlo code, we evaluated the impact of these new cross sections on yields of electron emission from solid gold irradiated by monoenergetic electron beams.

We obtained a mesoscopic potential value of -12.77 eV for our model of bulk metal gold, 27 % lower than the one commonly estimated from the Fermi energy. This result impacted on the inverse mean free path for plasmon excitations with a 10 % decrease for electrons in the range of 6 - 30 eV. Regarding electron emission yields, there was no impact of the new mesoscopic potential on the primary electron yields, but for secondary electrons, the emission yields were increased by a factor of up to two depending on the primary beam energy and thickness of the gold foil.

1. Introduction

Simulation of low-energy electron transport is a key factor in several scientific applications, such as the study of dose enhancement by gold nanoparticles in radiotherapy, where low energy electron flux is intimately related to the electron emission yields [1, 2]. Many Monte Carlo (MC) codes have been developed in order to perform simulations of electron transport through matter [3, 4]. However, most of these codes cannot be used when low energy electrons (< 100 eV) are considered, as the energy loss processes strongly depend on the electronic band structure of materials [5].

In the last years, our group has been working on the implementation of a physical model for electron transport down to low energy in solid metallic media [6]. Recently, a benchmarking of our Monte Carlo simulations code MDM was presented, performing an extensive comparison with available experimental data for gold-foil irradiated by electron beams.

In the model implemented in MDM, the potential in which kicked electrons evolve is decomposed in a mesoscopic part and a microscopic one. Like wave packets, such electrons evolve according to classical laws in the mesoscopic potential. Its total energy is, therefore, the sum of its kinetic energy

and its mesoscopic potential energy [7, 8]. The interaction with the microscopic potential is described through a collisional approach, for which the collision probabilities are sampled by the Monte Carlo simulation. These probability laws are known as inverse mean free paths or cross sections [9, 10]. The mesoscopic potential impacts on the free evolution of the moving electrons, but also on their collisions through the energy conservation law.

In absence of external forces (magnetic, electrostatic), the mesoscopic potential, $V_0(x, y, z)$, corresponds to the “smooth” part of the electrostatic potential created by the electrons and the nuclei of the solid. It is estimated by a local average of the solid potential in its ground state. For an infinite solid crystal, $V_0(x, y, z)$ is uniform and characterized by the constant value V_0 . For a finite solid, the potential may be set to V_0 inside the solid, vanishing to the vacuum level outside.

MC calculations such as electron yields depend on the cross sections on which these simulations are based. In our Monte Carlo models, the electron cross sections depend on the value of the mesoscopic potential that is used in the simulation [6]. In this context, the objective of this work was to improve the cross sections on which our MC code is based, some of which are still missing or imprecise. To do that, we calculated the three-dimensional electrostatic potential for a sample of bulk Au by using Density Functional Theory (DFT) calculations with VASP [11, 12, 13]. DFT and Kohn-Sham theory allows for an approximate resolution of the many-body electronic problem, in particular to determine the average electrostatic potential felt by one electron crossing a metallic bulk or a metallic surface. With the calculated electrostatic potential, we implemented a methodology to determine the mesoscopic potential V_0 within the solid. Using the calculated value of V_0 , we generated inelastic electron cross sections, to study its sensitivity to the potential. Finally, we performed MC simulations with MDM in order to evaluate the influence of the mesoscopic potential on experimentally available quantities, i.e., the electron emission from a foil of gold irradiated by an electron beam.

2. Materials and Methods

A. Electrostatic and mesoscopic potential calculations

A.1 Electrostatic potential calculation

The electrostatic potential of gold bulk was calculated by performing Density-Functional Theory calculations with the VASP package, version 5.3.5 [11, 12, 13]. PBE [14] with Grimme’s D3 semi-empirical dispersion corrected functional [15] (zero-damping formalism) was considered to describe the electronic exchange and correlation at the generalized gradient approximation (GGA) with van der Waals interactions (dispersion). The core-electrons were described by the projector-augmented wave [16] (PAW) pseudo-potentials (11 valence electrons per Au atom), and valence electrons were expanded in plane waves with a kinetic cut-off energy of 287 eV (HIGH precision in VASP). The FCC crystalline structure of gold bulk was described by using a k-point grid of $39 \times 39 \times 39$ (1540 irreducible k-points). The volume of the FCC bulk was relaxed completely with 10^{-7} eV for the convergence of the total electronic energy, leading to a lattice parameter (d) of 4.073 Å and a cohesion energy of -3.695 eV/at, in fair agreement with the experimental values (4.078 Å and -3.81 eV, respectively). A Methfessel-Paxton smearing was used for the calculation of the total electronic energy.

A.2 Mesoscopic potential calculation

In the model implemented in MDM, the total energy $U(x, y, z)$ of an excited electron is calculated by adding its kinetic energy and its mesoscopic potential energy, using the equation [6]:

$$U(x, y, z) = \frac{1}{2}mv^2 + qV_0(x, y, z) \quad (1)$$

where $V_0(x, y, z)$ is the mesoscopic potential at the position (x, y, z) , q is the electron charge, v is its velocity and m is its mass.

In this model, the mesoscopic potential, $V_0(x, y, z)$, represents the attractive background potential of the solid experienced by an excited electron. It is uniform inside the solid ($V_0(x, y, z) = V_0$) and it vanishes outside. To simplify the simulation, the vanishing is represented by a step function set to the vacuum level outside the solid and the constant value V_0 inside.

In previous calculations with MDM, V_0 was set according to the Sommerfeld model. Taking into account the energy of the Fermi level u_{Fermi} with regards to the vacuum level, V_0 verifies that $u_{\text{Fermi}} = E_{\text{Fermi}} + V_0$, where E_{Fermi} is the Fermi energy in the Sommerfeld model. For solid gold, we had $V_0 = -10.04$ eV for $u_{\text{Fermi}} = -4.59$ eV and $E_{\text{Fermi}} = 5.45$ eV.

According to its definition, the mesoscopic potential can be calculated performing a convolution between the electrostatic potential $V(x, y, z)$ and a Gaussian function $f(x, y, z)$ [7,8]. This last function can be written as follow:

$$f(x, y, z) = \frac{1}{(\sqrt{2\pi}\sigma)^3} e^{-\frac{(x^2+y^2+z^2)}{2\sigma^2}} \quad (2)$$

where σ represents the standard deviation, a parameter controlling the definition of the mesoscopic scale. According to this equation, the result of $V_0(x, y, z)$ will depend on the σ value used in the Gaussian function.

In order to calculate the mesoscopic potential, we have used the results of the electrostatic potential performed at the PBE-D3 level with the DFT approach (see Figure 1). As described in the previous section, this electrostatic potential was calculated at any point (x, y, z) of a 3D box of $4.07 \times 4.07 \times 4.07 \text{ \AA}^3$ with a grid of points of $24 \times 24 \times 24$, thus meaning a point density of $205 \text{ points.\AA}^{-3}$. To calculate the V_0 value, we built a bigger box by replicating the 4.07 \AA side 3D box 16 times in each of the x, y, z directions. We obtained a 3D box of $6.5 \times 6.5 \times 6.5 \text{ nm}^3$ with a point grid of $384 \times 384 \times 384$. Considering different values for the mesoscopic parameter σ , we calculated the Gaussian convolution. For each σ value we obtained $384 \times 384 \times 384$ values for the mesoscopic potential function. With these results, we selected the σ value taking into account that $V_0(x, y, z)$ was constant inside the solid. Once defined the standard deviation value, we calculated a value of the mesoscopic potential, V_0 , averaging over the points (x, y, z) of the grid where $V_0(x, y, z)$ reached an approximately constant value

B. Cross section calculation

In a previous work, all available models in MDM to generate elastic and inelastic electron cross section were described [6].

Concerning elastic interactions, two models were implemented in MDM. For high momentum transfer interactions, an atomic model was used. In this case, the cross sections were generated using the code ELSEPA [17], performing relativistic (Dirac) partial-wave calculations for scattering by a local central interaction potential. For low momentum transfer interactions, a phonon model was used. For inelastic interactions, two models were considered. For the deeply bound electrons (core electrons), the binary-encounter-Bethe (BEB) theory developed by Kim and coworkers [18, 19, 20] was used to calculate the core ionization cross section. For the weakly bound electrons (valence and conduction electrons), the model proposed by Ritchie and coworkers [21] was implemented to calculate the plasmon inverse mean free path.

We first studied the impact of V_0 on the cross section values, as inelastic cross sections directly depend on the mesoscopic potential value. In the BEB model, implemented in MDM to calculate the core ionization cross section, the binding energy of an electron is defined as $B_{\text{KIM}} = B + V_0$, where B is

the energy necessary to promote an electron to vacuum. In the model used to calculate the plasmon inverse mean free path, the doubly differential inverse mean free path is integrated over the momentum transfer and the energy loss of the projectile, from 0 to $E_{\text{kin}} + qV_0 - u_{\text{Fermi}}$, where E_{kin} is the kinetic energy of the projectile. Therefore, both core ionization cross section and plasmon inverse mean free path depend on the choice of the mesoscopic potential.

Concerning elastic cross sections calculations with ELSEPA code [6], we used the muffin tin option to mimic the potential of neighboring atoms in solid state. We chose the radius of the Muffin-Tin model equal to one-half of the interatomic distance used in the electrostatic potential calculations.

In order to evaluate the impact of the mesoscopic potential in the cross section, we calculated the core ionization cross section and the plasmon inverse mean free path using the value of V_0 obtained in this work and we compared the results with previous calculations.

Finally, we evaluated the impact of this variations in the total electron cross section. To do that, we compared the results calculating the relative difference in the total cross section, using the following equation:

$$\text{relative difference (\%)} = \frac{|\sigma_0' - \sigma_0| * 100}{\sigma_0} \quad (3)$$

where σ_0' is the total cross section calculated with the potential V_0' and σ_0 is the total cross section calculated with the potential V_0 .

C. Monte Carlo simulations: electron emission yields

With the objective of evaluating the impact of the generated cross sections in MC simulations, we performed a series of simulations of the electron emission following the irradiation of solid gold by electrons. Precisely, we repeated the simulations performed in a previous work [6] to compare MDM results with electron yields obtained experimentally by Reimer and coworkers [22], but using the cross sections for inelastic scattering calculated with the new value of V_0 . As in the previous work, we defined the electron yield of a material under electron irradiation as the number of emitted electrons per incident electron. The primary electrons were defined as electrons with energies greater than 50 eV, and the secondary electrons with energies lower than 50 eV. In the experiment considered, a gold layer was surrounded by vacuum. The foil was irradiated with an electronic beam normally to de surface. Different irradiations were performed considering various energies and foil thickness.

In our simulations, 50000 electrons were sent in each irradiation. We calculated primary backscattered and transmitted electron yields, and secondary backward and forward electron yields. Finally, we compared the results with previous simulations and with experimental data.

3. Results and discussions

A. Electrostatic and mesoscopic potential calculation

Figure 1 shows electrostatic and mesoscopic potential calculations along the axe defined by $(x, y) = (3.25 \text{ nm}, 3.25 \text{ nm})$. Note that, 3.25 nm is equal to one-half of the box size used in the calculations and the position $(x, y, z) = (3.25 \text{ nm}, 3.25 \text{ nm}, 0)$ corresponds to the position of an atom. The σ value selected for the mesoscopic potential calculation in this figure corresponds approximately to two third of the lattice parameter (d). As it was expected, the peaks of the electrostatic potential disappeared after the Gaussian convolution and the mesoscopic potential tended to be constant within the solid. However, there were some small oscillations in V_0 (coincident with the positions of the peaks in the electrostatic potential), which could be flattened using a different value of the σ parameter.

Figure 2 presents the mesoscopic potential calculated for three σ values: 0.17 nm, 0.19 nm and 0.21 nm. This figure shows that the oscillations in the mesoscopic potential were smaller when the σ value

was increased. For σ equal to 0.21 nm, the mesoscopic potential reached a flattened form in the region inside of the solid.

We calculated for each σ value showed in Figure 2, an average value for the mesoscopic potential taking into account the points (x, y, z) of the grid where V_0 was approximately constant. The calculated value for σ equal to 0.21 nm was equal to -12.77 eV. The choice of the σ value is a compromise. It has to be chosen large enough to reduce significantly the microscopic fluctuation of the potential, but small enough to take account for the geometry of the solid and in particular its interfaces. The value 0.21 nm seems to achieve this compromise. In parallel, we obtained the value of V_0 calculating an average value of the electrostatic potential 3D matrix for 1 atom. This value was equal to -12.77 eV. Therefore, this result showed that the value obtained in the convolution represented the mean value of the electrostatic potential. As we mentioned in Section 2.A, the previous value used in MDM for the cross section calculations was equal to -10.04 eV. The relative difference between this value and our calculated $V_0 = -12.77$ eV was approximately 27%.

B. Cross section generation

Figure 3 shows the core ionization cross section calculated for $V_0 = -10.04$ eV and for $V_0' = -12.77$ eV. The cross sections were represented as a function of the total energy of the electron, defined in equation 1. The results showed that, for V_0' , the cross section was increased and there was a shift towards the region of lower energies.

Figure 4 shows the plasmon inverse mean free path calculated for $V_0 = -10.04$ eV and for $V_0' = -12.77$ eV. The results showed differences in the energy range from 15.5 eV to 50 eV, where the values obtained for $V_0 = -10.04$ eV were higher. This effect was related to the condition imposed in the model, $E_{\text{kin}} + qV_0 - u_{\text{Fermi}} > 0$. This constrain is necessary to respect for the Pauli principle, which exclude for both the incident and secondary electrons after interaction the occupation states below the Fermi level. For $V_0 = -10.04$ eV, E_{kin} must be greater than 5.45 eV, and for $V_0' = -12.77$ eV, E_{kin} must be greater than 8.18 eV.

Figure 5 presents the relative difference in the total electron cross section as a function of the electron kinetic energy. This relative difference reached the value of 10% for the energy of 10 eV, due to the effect of the plasmon inverse mean free path. For energies lower than 6 eV or greater than 30 eV, the values of this relative difference remained lower than 1%. The change in core ionization cross section had a negligible impact on the calculation of the total cross section. The differences found for the plasmon inverse mean free path, could play an important role in the Monte Carlo simulations of low energy electrons.

C. Monte Carlo simulations: electron emission yields

We investigated the impact of the calculated cross sections on the electron emission yields calculations with MC simulations. Figure 6 shows the results obtained with MDM for the electron emission yields. Figures 6.a) and 6.b) present the primary backscattered and transmitted electron yields respectively. Figures 6.c) and 6.d) present the secondary backward and forward electron yields respectively.

According to the results showed in figures 6.a and 6.b, the change in V_0 does not have any influence on the primary electron emission yields. It was expected because, for high electron energy, the cross section was not impacted by the changes in V_0 .

Figures 6.c and 6.d show that the backward and forward secondary yields were increased for $V_0 = -12.77$ eV. Regarding the backward yields, our results were close to the experimental ones, for all the energies and thickness studied. For the case of forward yields, our results overestimated the previous ones. The increase in the secondary electron yields for $V_0 = -12.77$ eV can be explained analyzing the relative difference in total cross sections presented in Figure 5. For electron kinetic energies greater than 6 eV and lower than 30 eV, the cross section for $V_0 = -10.04$ eV was higher than that for $V_0 = -12.77$ eV.

12.77 eV. For this reason, for $V_0 = -12.77$ eV, the interaction probability of secondary electrons was decreased, and consequently, the probability that one of those electrons leaves the foil was increased. Depending on the electron energy and the foil thickness, the secondary electron emission yields for $V_0 = -12.77$ eV reached values that doubled the previous calculated ones. Therefore, the change of V_0 value had a significant impact in the Monte Carlo simulation results for the transport and the emission of low-energy electrons.

4. Conclusion

In this work, we evaluated the mesoscopic potential of solid gold and its influence on electron emission yields in order to improve Monte-Carlo simulation of electron transport in matter and improve the cross sections. We implemented a methodology to calculate the mesoscopic potential based on the electrostatic potential predicted by DFT calculations in gold bulk. This new value of V_0 was equal to -12.77 eV, which was 27% lower than the previous one. We calculated inelastic inverse mean free path considering our new value of V_0 and observed a significant impact for plasmon excitation by electrons in the range from 6 to 30 eV (up to 10%). While the transport of fast electrons was found insensitive to V_0 change, the secondary electron emission was increased by a factor up to two. Secondary backward yields were improved with regard to experimental data, but, secondary forward yields were overestimated for all the energies and thickness studied.

The methodology implemented in this work to calculate the V_0 value can be extended to other applications. In a future work, we will use these methods to generate the V_0 value for gold nanoparticles, in order to generate the cross sections and to perform nanodosimetry calculations for the study of dose enhancement by gold nanoparticles in radiotherapy.

Acknowledgments

This work was supported by the LABEX PRIMES (ANR-11-LABX-0063) of Université de Lyon, within the program ‘Investissements d’Avenir’ (ANR-11-IDEX-0007) operated by the French National Research Agency (ANR).

The authors thank GENCI in Paris (project 609) and PSMN in Lyon for CPU time and assistance. The authors thank the CPER/SYSPROD 2015-2022 project (N°2019-AURA-P5B) and AXELERA Pôle de Compétitivité for financial support (PSMN Data Center).

References

- [1] J. Pierron et al., “Electron emission yield for low energy electrons: Monte Carlo simulation and experimental comparison for Al, Ag, and Si”, *Journal of Applied Physics* 121 215107, 2017.
- [2] Y. T. Yue et al., “Monte Carlo simulation of secondary electron and backscattered electron images for a nanoparticle-matrix system”, *Journal of Physics D: Applied Physics*, 38 1966-1977, 2005.
- [3] D. Pelowitz, MCNP6 User’s Manual, Version 1.0, LA-CP-13-00634, Rev. 0, Los Alamos National Laboratory, New Mexico, USA, 2013.
- [4] S. Agostinelli et al., “GEANT4: A simulation toolkit”, *Nucl. Instrum. Meth. A* 506 250-303, 2003.
- [5] W. G. Shin et al., “Development of a new Geant4-DNA electron elastic scattering model for liquid-phase water using ELSEPA code”, *Journal of Applied Physics* 124, 224901, 2018.
- [6] F. Poignant, et al., “Theoretical derivation and benchmarking of cross sections for low-energy electron transport in gold”, *The European Physical Journal Plus*. 135 (4), 2020.
- [7] M. Beuve et al., “Monte Carlo simulation of electron emission induced by Swift highly charged ions: beyond the linear response approximation”, *The European Physical Journal D* 21, 125-135, 2002.
- [8] M. Beuve, thèse de l’université de CAEN, 1999.

- [9] A. Jablonski et al., “NIST Electron Elastic-Scattering Cross-Section Database Version 4.0”, NIST Standard Reference Database Number 64, National Institute of Standards and Technology, Gaithersburg MD, 20899, 2016.
- [10] R. G. Newton, “Scattering Theory of Waves and Particles”, McGraw Hill, 1966.
- [11] G. Kresse, et al., “Ab-initio Molecular Dynamics for Liquid Metals”, *Phys. Rev. B*, 47, 558, 1993.
- [12] G. Kresse, et al., “Efficiency of Ab-initio Total Energy Calculations for Metals and Semiconductors Using a Plane-wave Basis Set”, *Comput. Mat. Sci.* 6, 15-50, 1996.
- [13] G. Kresse, et al., “Efficient Iterative Schemes for Ab-initio Total-energy Calculations Using a Plane-wave Basis Set”. *Phys. Rev. B*, 54, 11169, 1996.
- [14] J. P. Perdew et al., “Generalized Gradient Approximation Made Simple”, *Phys. Rev. Lett.* 77, 3865, 1996.
- [15] S. Grimme et al., “A consistent and accurate ab initio parametrization of density functional dispersion correction (DFT-D) for the 94 elements H-Pu”, *J. Chem. Phys.*, 132, 154104, 2010.
- [16] G. Kresse et al., “From Ultrasoft Pseudopotentials to the Projector Augmented-wave Method”, *Phys. Rev. B* 59, 1758, 1999.
- [17] F. Salvat et al., “ELSEPA-Dirac partial-wave calculation of elastic scattering of electrons and positrons by atoms, positive ions and molecules”, *Computer Physics Communications* 165 157-190, 2005.
- [18] Y.-K. Kim et al., Binary-encounter-dipole model for electron transport ionization”, *Phys. Rev. A* 50, 3954-3967, 1994.
- [19] W. Hwang et al., “New model for electron-impact ionization cross sections of molecules”, *J. Chem. Phys.* 104, 2965.
- [20] B. Gervais et al., “Numerical simulation of multiple ionization and high LET effects in liquid water radiolysis”, *Radiation Physics and Chemistry* 75 495-513, 2006.
- [21] R. Ritchie, “Interaction of charged particles with a degenerate Fermi-Dirac electron gas”, *Phys. Rev.* 114 644-654, 1959.
- [22] L. Reimer et al., “Secondary electron emission of 10-100 keV electrons from transparent films of AL and Au”, *Journal of Physics D: Applied Physics* 10 805, 1977.

Figures

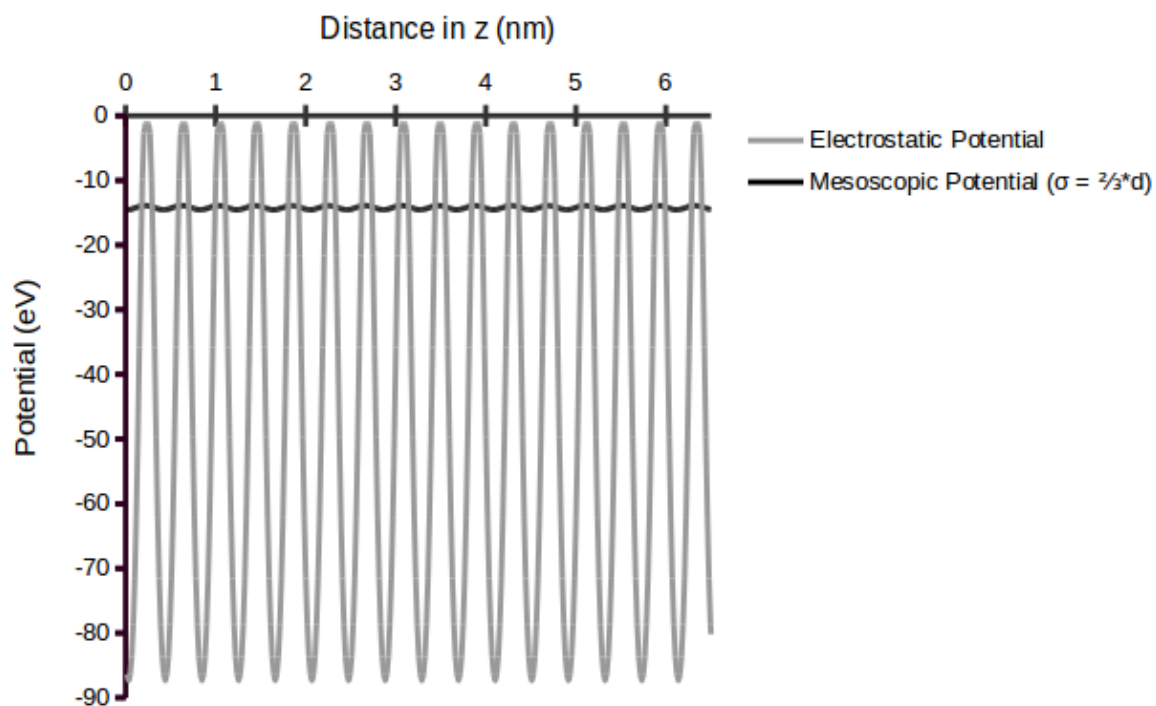


Figure 1: electrostatic (DFT-D3 level) and mesoscopic potential as a function of the distance in z at $(x,y)=(3.25 \text{ nm}, 3.25 \text{ nm})$.

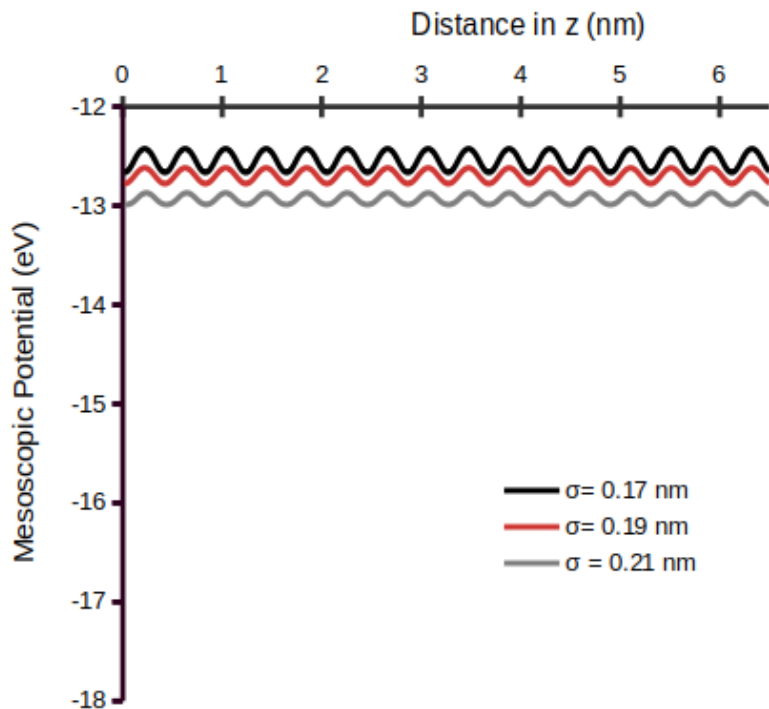


Figure 2: mesoscopic potential for different σ values as a function of the distance in z at $(x,y)=(3.25 \text{ nm}, 3.25 \text{ nm})$.

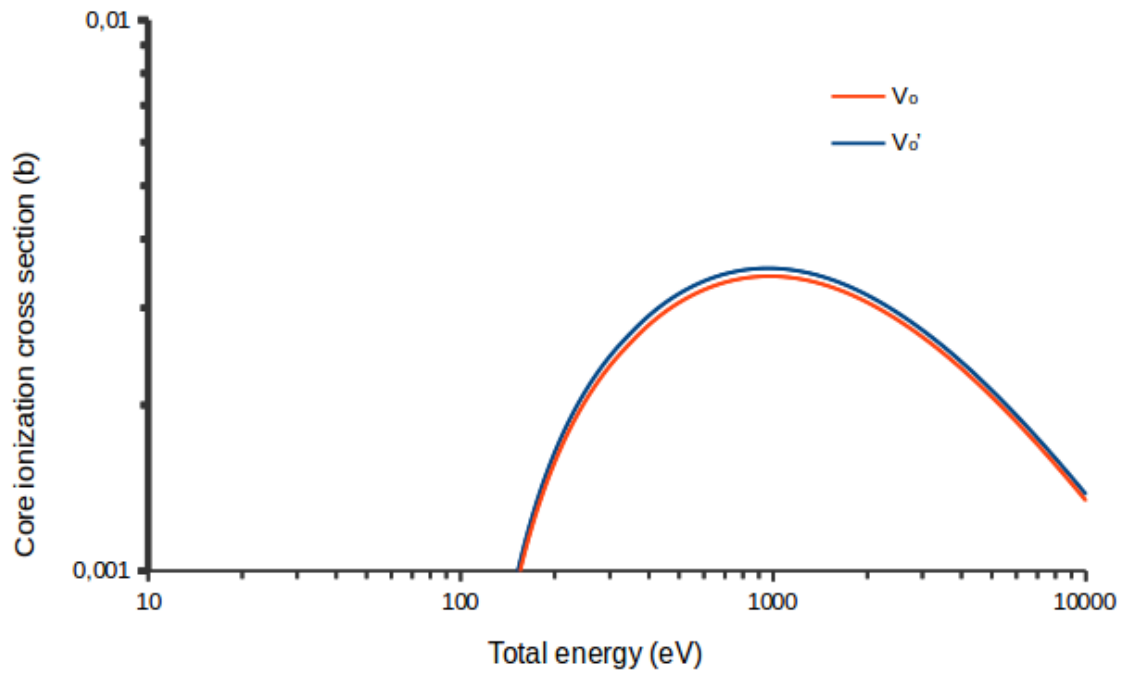


Figure 3: core ionization electron cross section as a function of the projectile energy.

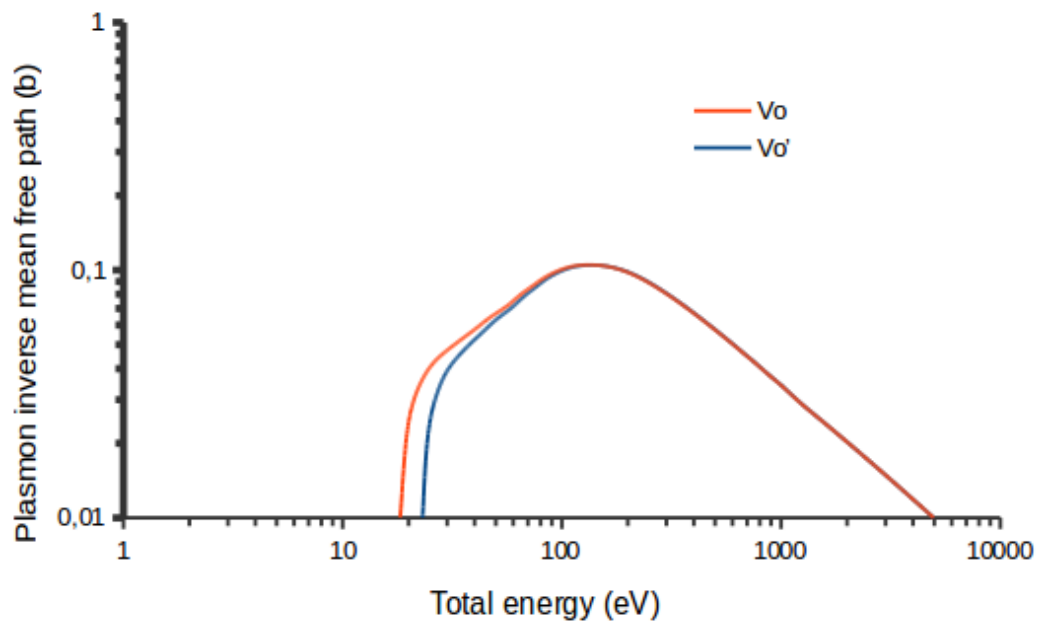


Figure 4: Plasmon inverse mean free path as a function of the projectile energy.

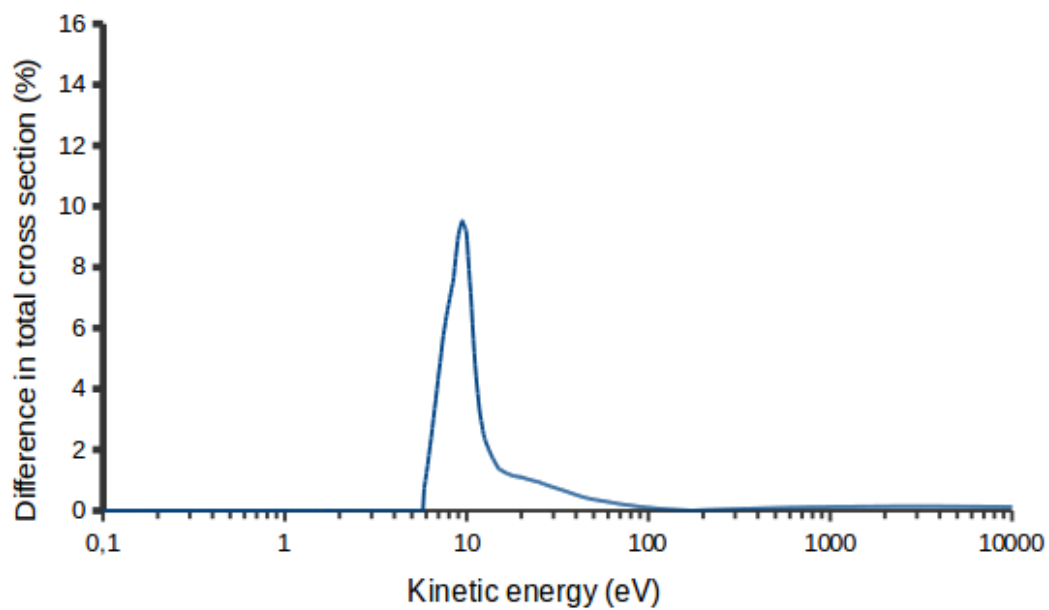


Figure 5: Relative difference in the total cross section as a function of the projectile kinetic energy.

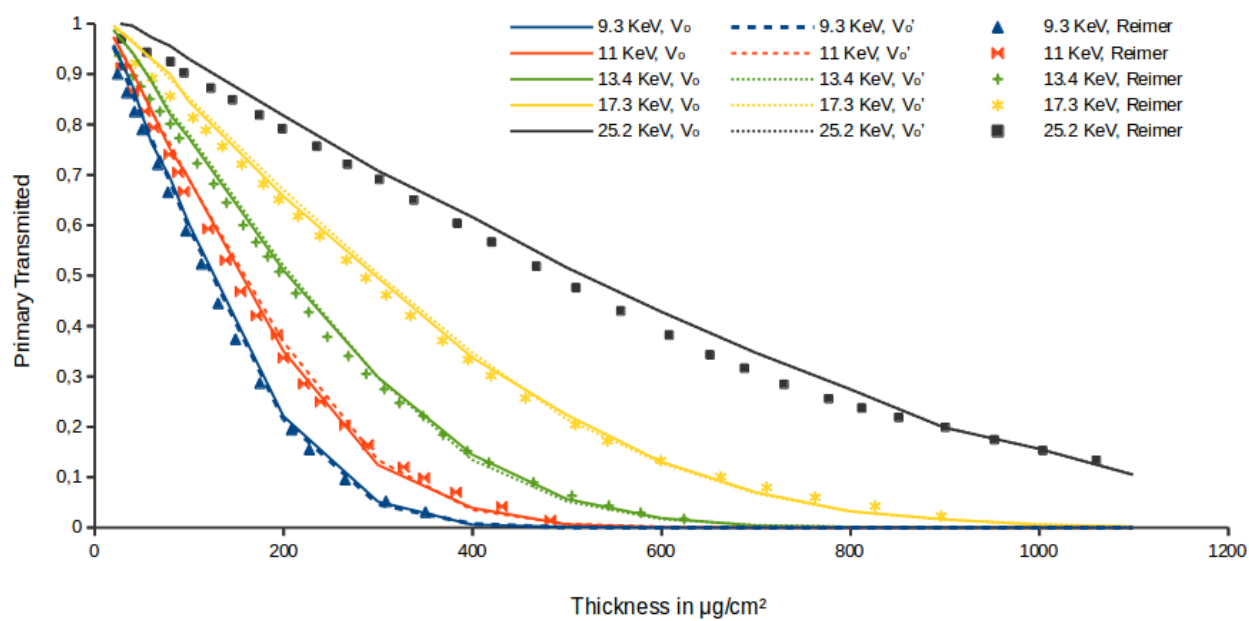


Figure 6.a: Primary transmitted electron yields for $V_0 = -10.04$ eV, $V_0' = -12.77$ eV and experimental data.

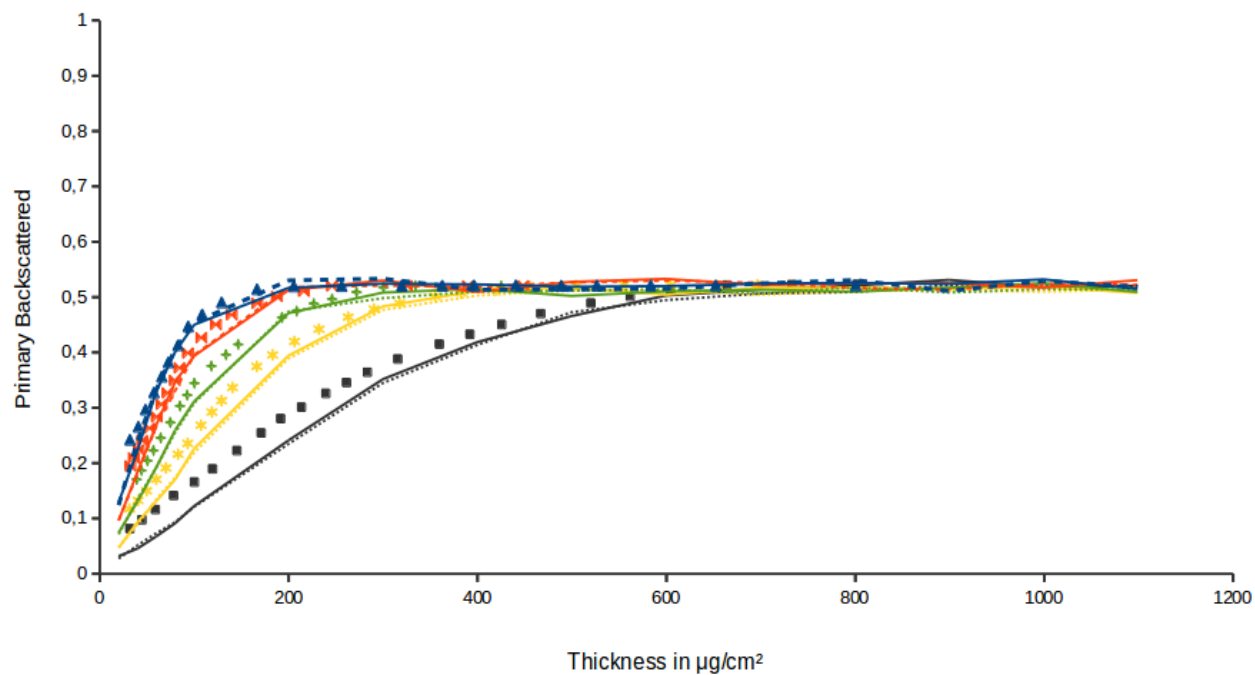


Figure 6.b: Primary backscattered electron yields for $V_0=-10.04$ eV, $V_0'=-12.77$ eV and experimental data.

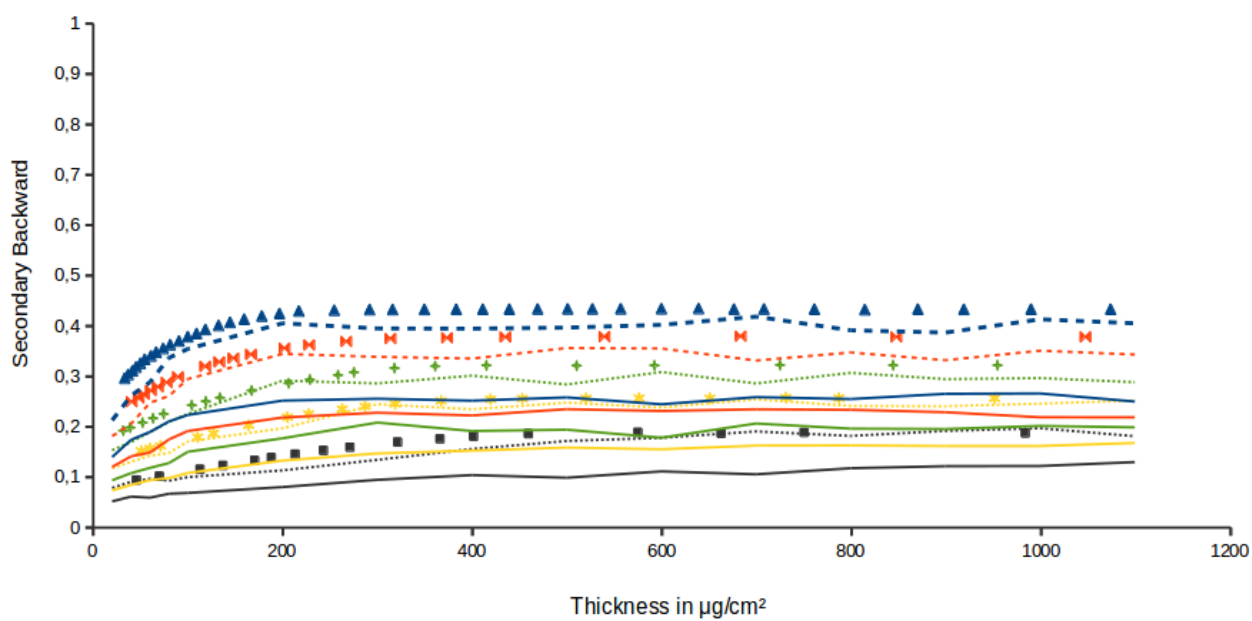


Figure 6.c: Secondary backward electron yields for $V_0=-10.04$ eV, $V_0'=-12.77$ eV and experimental data.

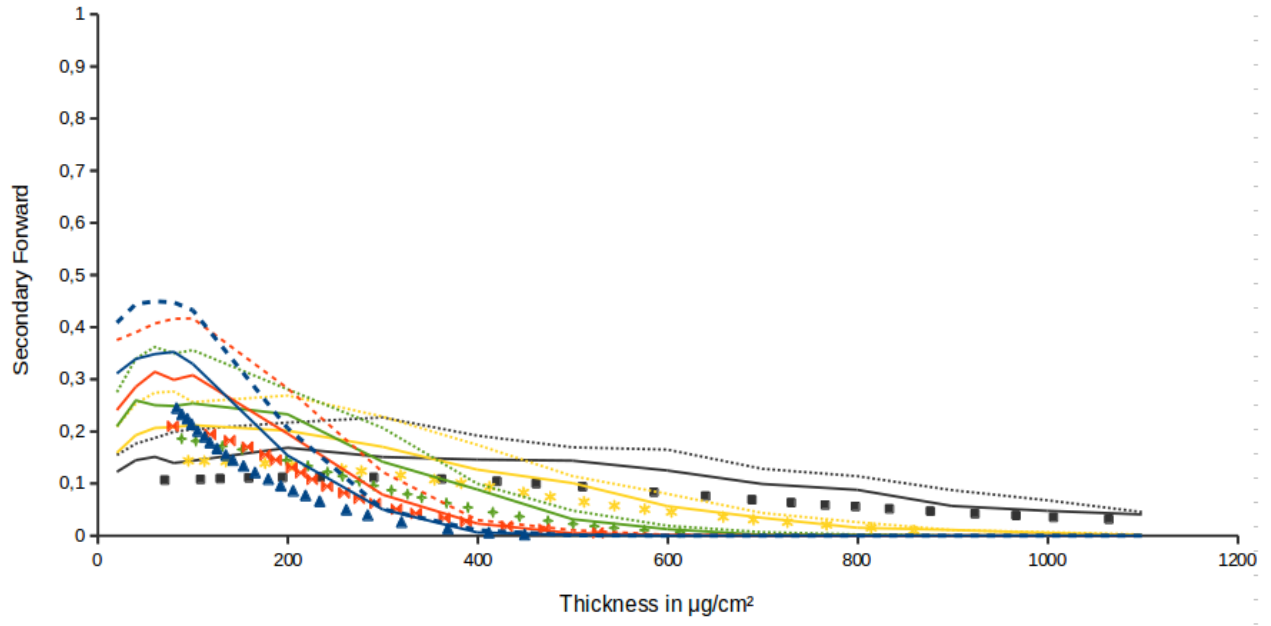


Figure 6.d: Secondary Forward electron yields for $V_0 = -10.04$ eV, $V_0' = -12.77$ eV and experimental data.